Soft-Tipped Sensor with Compliance Control for Elasticity Sensing and Palpation

Duncan G. Raitt[1], Mahmud Huseynov[1], Shervanthi Homer-Vanniasinkam[1], Helge A. Wurdemann[1], *Member, IEEE*, and Sara-Adela Abad[1,2], *Member, IEEE*

***Abstract*—Stiffness sensing and palpation are essential for understanding object properties, including tissue health and fruit ripeness. Currently, there is limited research on using soft-tipped sensors for stiffness sensing and dynamic palpation. To address these challenges, we investigate how the pressure modulated optical tracking (PMOT) sensor can use compliance control to quantify tissue stiffness and detect margins in samples through dynamic palpation. Results show that the PMOT sensor modulus of elasticity sensing range is from 4.20 kPa up to 177.62 kPa. Across all untrained samples, elasticity was measured with a root-mean-square error (RMSE) of 7.72%. Further, it is shown that the sensor can locate margins between 13.4 kPa and embedded 29.3 kPa materials during palpation. When mounted on a linear rail, averaged for the direction of travel, the sensor's signal-to-noise ratio (SNR) was up to 39.5:1. Participants used the sensor to locate embedded margins in a teleoperation environment with visual feedback. This was achieved with an accuracy of 96.5%.**

***Index Terms*—Stiffness Sensing, Elasticity Sensing, Palpation, Force Sensing, Tactile Sensor, Soft Sensor, Haptic Sensor**

I. Introduction

STIFFNESS sensing is essential for understanding the objects with which a robot is operating. In grasping and manipulation tasks, objects with different stiffnesses should be handled differently, to maintain maximal control. Whilst in medical robotics, stiffness can convey information about tissue types and tissue health, because unhealthy tissue often has a different stiffness than that around it. For example, breast cancer tissue can be ten times stiffer than normal breast tissue [1]. To ensure their users can be fully informed, sensors should be able to measure sample stiffness numerically and detect changes in stiffness during sensor motion.

In the literature, stiffness is used to refer to two different measurements. Traditionally, stiffness refers to the spring constant (k) of an object [2]–[5]. On the other hand, researchers have used stiffness as a shorthand for tissue stiffness which is measured as the modulus of elasticity (E) of a material [1], [6]–[11]. Whilst k describes the property of a structure and E describes the property of a material, the two are linked by (1) [10].

This work was supported by the U.K. Engineering and Physical Sciences Research Council (EPSRC) under Grant: EP/S014039/1 and by the UCL Therapeutic Acceleration Support Fund under Grant No. 184646.

[1] D.G. Raitt, M. Huseynov, S. Homer-Vanniasinkam, H.A. Wurdemann, S.-A. Abad are with the Department of Mechanical Engineering, UCL, London, WC1E 7JE, UK. (e-mail: {duncan.raitt.19, s.homer-v, h.wurdemann, s.abad-guaman}@ucl.ac.uk).

[2] S.-A. Abad is with the Facultad Agropecuaria y de Recursos Naturales Renovables, Universidad Nacional de Loja, Loja, 110101, Ecuador.

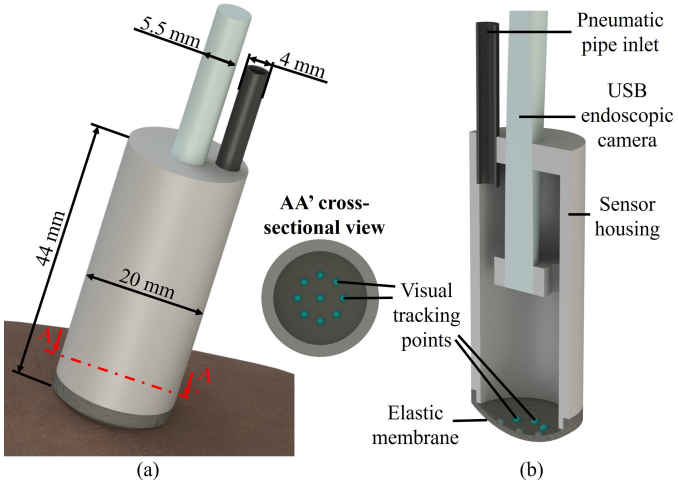

Fig. 1. Pressure modulated optical tracking (PMOT) sensor dimensions and components. (a) Side view of our sensor sensing tissue stiffness with dimensions. (b) 3D cross-sectional view of our sensor with component labels. An endoscopic camera tracks the position of points on the inner surface of the membrane. Allowing displacement to be measured during pressurisation and palpation.

$$k = \frac{EA}{L_0} \tag{1}$$

Where A is the area and L_0 original length of an object. Therefore, one is directly proportional to the other when measuring objects of the same dimensions.

Several techniques can be used to measure stiffness. The force and displacement of an actuator interacting with the sample can be tracked [6], [12]. How the sample conforms as it is indented or aspirated can be measured [7], [9], [13], [14]. The shift in resonance frequency of a device in contact with a sample can be analysed [8], [15]. The ratio of forces acting on two half plates of different compliance under shear forces [16]. The deformation of two or more indenters of different compliance can be compared [2], [17]. However, none of these sensors have been used in dynamic palpation to find where tissue changes in an object. Other sensors have been shown to detect changes in stiffness when they are moved across the tissue during dynamic palpation. In most sensors, this is done by measuring force as the sensor is moved [18]–[23]. However, these sensors require additional information from external sensors to quantify stiffness. For example, Jenkinson et al. produced a sensor that could detect changes

0000–0000/00$00.00 © 2021 IEEE

in stiffness when repeatedly pressed across the tissue, but could only characterise stiffness when pushed against a sprung surface with a known displacement [3]. The need for external position tracking reduces its stiffness-sensing ability when mounted on robots with less accurate kinematic tracking. A sensor with the capability to measure stiffness without external position sensing and carry out dynamic palpation is studied by Faragasso et al. [4], [24]. However, this sensor interacts using stiff-tipped indenters, which may damage tissue [25], [26]. On the other hand, it has been shown in previous work [27] that the pressure modulated optical tracking (PMOT) sensor (Fig. 1) can measure force with a variable range through compliance control of a soft membrane.

In this paper, we explore new sensing modalities for this sensor and further expand its capabilities. We demonstrate that this soft-tipped sensor is also capable of *i)* quantifying sample elasticity without an external position reference and *ii)* sensing changes in stiffness during dynamic palpation. To achieve this, we present an innovative method that measures elasticity by changing the compliance of a membrane and measuring its deformation.

Section II gives a thorough review and comparison of current stiffness sensing techniques. In Section III, an overview of our sensing method is given followed by experiments in Sections IV, V, and VI. These experimental sections discuss results with regards to stiffness sensing as well as dynamic palpation (with human participants through teleoperation). Section VII concludes the findings.

II. Stiffness Sensing Literature Review

To better understand the capabilities of stiffness sensors, a literature review was carried out. Stiffness sensors measuring the force-displacement relationship were developed by Hassanbeiglou et al. and Afshari et al. [6], [12]. In [6], tactile switches were mounted on a trapezoid above a force sensor, allowing the indentation depth and force to be measured. This was used by the authors to observe how the sensor responded to tissue samples of different softness at different indentation rates. A sensing probe which actuated a known displacement into a tissue and measured the resulting forces is investigated in [12]. This showed distinct Force displacement graphs for samples of different stiffness. Neither sensor is shown to be able to locate embedded objects in dynamic palpation and their ability to compensate for shear forces is unknown. The methodology in [12] describes a dynamic palpation experiment, however, only data from static probing into the sample are given in the results. Both of these sensors interact using stiff components.

Tissue conformation during aspiration or indentation has been used to calculate stiffness [7], [13]. The probe used in [7] measured the aspiration pressure and displacement of the tissue into the sensor. This was shown to be safe performing in vivo trials. It could estimate modelling coefficients of a synthetic sample and tissues when inverse finite element analysis was applied. This sensor uses stiff components to press against the edge of the aspirated area. Gubenko et al. demonstrated a tissue stiffness sensor that measures stiffness by measuring the vertical displacement of a central mirror and recording the contact area radius using a camera [13]. These measurements were compared to a finite element model to measure the tissue stiffness of two samples, around 2300 kPa and 200 kPa in elasticity. These were calculated with errors ”above 10%” and ”near 5%”. This sensor was soft-tipped. Nguyen et al. developed a sensing chip which used three piezoresistive cantilevers to measure tissue stiffness [9]. One cantilever was placed at the centre of the chip whilst the other two were positioned at the edge. These were then covered by an elastic pad. Softer tissues would conform more to the sensor, putting a higher force on the edge cantilevers relative to the centre cantilever. This difference could be measured from the cantilever resistances. The sensor was pressed against six samples that vary in elasticity from 57 kPa to 3.2 GPa. Each produced a distinct plot when resistance ratios were plotted. Neither sensor was tested in dynamic palpation or with shear forces.

Tissue conformation properties were also used by Yuan et al. to allow the Gelsight sensor to sense hardness [14]. The sensor was pushed into samples of different hardness whilst recording the motion of the sensor’s surface. The deformation was input to a neural network over several frames to find the sample hardness. Whilst stiffness is often perceived alongside hardness, it is important to note that in soft materials these two properties do not always correlate [28], [29]. The samples used ranged in hardness 00-8 to 00-87. These were made from elastomers which range in elasticity from around 55 kPa to around 827 kPa. Samples of trained shapes but untrained hardness were measured with a root-mean-square error (RMSE) of 00-5.18, 5.95% of range. The Gelsight sensor has also been shown to be able to measure forces when interacting with stiff objects and detect embedded nodules when statically held against a sample [30], [31]. However, it has not been shown if this sensor can be used in dynamic palpation to locate changes in stiffness and locate embedded objects in soft materials.

Shifts in resonant frequency have also been used to measure tissue stiffness. Omata et al. showed that the shift in resonant frequency of the sensor at a set indentation pressure correlated with Young’s modulus and spring constant [15]. Samples between 10 kPa and 100 GPa in elasticity were tested. Zhang et al. tested a resonance sensor which could work at angles up to 45° to categorise samples of different stiffness [8]. Samples with hardnesses increasing in steps from 9.3% to 87.5% were correctly categorised at a rate of 92%. It should again be noted that hardness and stiffness may not correlate. Both of these sensors are hard-tipped and have not been tested in dynamic palpation.

Comparing the deformation of indenters of different compliance has been used to sense stiffness. Faragasso et al. measured the displacement of two pairs of indenters on springs of different compliance using a camera [2]. This was tested on four silicon samples, 1 time each. These samples had spring stiffnesses between 0.0856 N/m and 2.2373 N/m and were calculated with errors between 1% and 5% of sample spring stiffness. The mean error was 3.5% of sample spring stiffness. This sensor was adapted to fit on an endoscope in

TABLE I
LIST OF AVAILABLE STIFFNESS SENSORS

Paper	Measurement	Sample Range	Sensor accuracy	Tip material	Dynamic palpation
[6]	Sensor response	Not assessed	Not assessed	Stiff	Not tested
[12]	Sensor response	Not assessed	Not assessed	Stiff	Not tested
[7]	Model Parameters	Not assessed	Not assessed	Stiff	Not tested
[13]	Elasticity	200 kPa & 2300 kPa	≈5% & >10% of sample stiffness	Soft	Not tested
[9]	Sensor response	57 kPa - 3.2 Gpa	Not assessed	Hybrid	Not tested
[14]	Hardness	00-8 - 00-87 (≈55 kPa - 827 kPa)	RMSE of 00-5.18, 5.95% of range	Soft	Not tested
[15]	Sensor response	10 kPa - 100 Gpa	Not assessed	Stiff	Not tested
[8]	Hardness categorisation	00-24 - 00-75	92% correctly categorised	Stiff	Not tested
[2]	Spring stiffness	0.0856 N/m - 2.2373 N/m	Errors of 1%-5% of sample stiffness. Mean error of 3.5%	Stiff	Not tested
[17]	Spring stiffness	0.0856 N/m	Error of 5.386% of sample stiffness	Stiff	Not tested
[4]	Spring stiffness	0.29 N/m & 0.62 N/m	Max error of 6.4% of sample stiffness	Stiff	Mapped stiffness
[16]	Elasticity	40 GPa	Not assessed	Hybrid	Not tested

[17]. It used four beams, three of a high compliance and one of a low compliance, the ends of which were tracked using the endoscope. This was tested on a single phantom with an error of 5.386%. Both of these sensors interacted using stiff components and were not tested in dynamic palpation.

Faragasso et al. adapted their stiffness sensors and force sensor from [32] to be usable for dynamic palpation [4]. This sensor used three high-compliance sprung indenters arranged around a low-compliance sprung indenter. Results showed the spring stiffness of 0.29 N/mm and 0.62 N/mm samples could be measured at angles up to 20° with maximum errors of 6.4% of sample stiffness. This device could create a map of tissue stiffness in handheld and robotic dynamic palpation. The sensor used stiff indenters to interact with the sample.

Nagatom and Miki created a sensor that measured the sample stiffness by comparing the stress on materials of different compliance during shear forces [16]. Four strain gauges were arranged around a contact pin, two embedded in a lower compliance PDMS and two embedded in a higher compliance PDMS. When loaded under shear loads the sensor measured the probes stiffness as around 40 GPa. The sensor was not tested with samples in the magnitude of human soft tissues or with lubricants representing fluids found in in vivo palpation. The sensor used a hybrid tip made of both stiff and soft materials. The sensor was not tested in dynamic palpation tasks where the stiffness changes and could likely not detect embedded objects due to only measuring the elasticity from horizontal interactions with the tissue surface.

The aforementioned stiffness sensors are summarised in Table I, alongside the measured stimulus, the range of samples tested, sensor accuracy performance metrics, the stiffness of the tip components interacting with the tissue, and whether any dynamic palpation tasks were carried out with each sensor. This reinforces that no soft-tipped sensor has been shown to be able to quantify sample stiffness and carry out dynamic palpation. We remark that many papers only reported the sensor's response to samples of different stiffness and did not attempt to measure the sample stiffness with the sensor. When sample stiffness was measured, authors used different metrics to characterise sensor performance. To allow the stiffness measurement results from this paper to be compared across the literature, results will be reported as the root-mean-square error (RMSE) and mean absolute error (MAE) compared to each sample and across the sensor's range, additionally, the non-repeatability will be given.

III. SENSING PRINCIPLE AND MECHANICAL DESIGN

A. Sensing Principle

The pressure modulated optical tracking (PMOT) stiffness sensor measures elasticity by varying its internal compliance and measuring the resulting tissue and membrane deformation. The compliance of the sensor increases with pressure due to two main factors: firstly, the increase of the internal pressure causes the internal air mass to rise in line with the ideal gas equation in (2), leading to an increase in internal stiffness [33]. Secondly, the membrane increases in strain as the internal pressure grows, causing the membrane to stiffen. On demand compliance control has been applied to multiple of soft robots [34].

$$n = \frac{PV}{RT} \tag{2}$$

Where n is the number of moles of gas present, P is the internal pressure, V is the internal volume, R is the ideal gas constant, and T is the temperature.

The method of measuring the deformation of at least two springs of different stiffness to find the stiffness of an object is used by Faragasso et al. [2], [17]. When two springs of different stiffness, attached to a common base plate, are placed into normal contact with a flat tissue sample, the spring constant of the tissue can be calculated using (3) [2]. Assuming that there is no interaction between the two affected areas of tissue.

$$k_s = \frac{F_1 - F_2}{\Delta d} = \frac{k_1 \Delta x_1 - k_2 \Delta x_2}{\Delta d} \tag{3}$$

Where k_s, k_1, and k_2 are the spring constant of the sample and two springs, F_1 and F_2 are the forces between the springs and the tissue, Δd is the difference in embedded depth between the two springs and Δx_1 and Δx_2 are the deformations of the two springs.

As long as the sensor and tissue are held rigid, the PMOT sensor can measure tissue stiffness through the same principle with only a single contact point. The PMOT sensor can set its compliance to more than two values, allowing the deformation to be related to the tissue stiffness. The compliance of the membrane tip at each internal pressure is proportional to the two spring stiffnesses, k, in (3). The difference between the

position of the membrane tip and its position at the same internal pressure when not in contact with the membrane would be proportional to the deformations of the two springs, Δx, in (3). An approximation of spring stiffness could be calculated from (3) using the relationship between membrane tip displacement, force, and tracking point displacements at each internal pressure. These relationships could be obtained using a linear rail and force sensor in line with the experiments in [27]. However, this may not fully capture the interaction between the tissue and the dome-shaped membrane as forces would not be applied in the same manner as a flat surface on the membrane tip. Therefore, a regression neural network (NN) was used to account for the more complex relationships. Biomedical literature measures tissue stiffness in the form of modulus of elasticity [10], [11], [35]. So, we used this variable rather than the spring constant to allow for cross-referencing.

The PMOT sensor can also perform dynamic palpation when working as a force sensor. During palpation, the sensor is moved across the tissue. As the stiffness of the tissue increases, the force acting on the sensor increases. By varying the compliance of the sensor, its range can be adapted to the tissue stiffness.

B. Mechanical Design and Fabrication

The PMOT sensor, depicted in Fig. 1, is built from a stiff housing with an elastomer membrane on one end. A camera and pneumatic piping are inserted into the opposite end. The housing is printed from Formlabs Tough 2000. The membrane was cast from Ecoflex 00-50, mixed with a ratio of 5 g part A to 5 g part B, to 0.2 ml of Silc Pig black. This is stiffer than the membrane used in [27] to reduce the effects of shear forces during palpation. Hemispherical tracking points, 1.4 mm in diameter, were cast on the membrane's inner surface and painted with a mixture of Smooth-On Psycho Paint and Smooth-On Silc Pig Cyan. These were arranged one in the centre and eight in a circle with a radius of 4 mm around it as shown in Fig. 1b. The membrane was glued to the housing at its edge and wrapped with Polytetrafluoroethylene (PTFE) tape to ensure an air-tight seal.

The pneumatic pipe and camera were sealed in place using silicone sealant. The 4 mm diameter pneumatic pipe was connected to an SMC ITV0010 pressure regulator which could be used to control the sensor's internal pressure. The 5.5 mm diameter, 1.3 MP, ROTEK USB Otoscope camera was connected to a computer. The tracking points' positions are extracted from each frame using the OpenCV library. A 7 by 7 blur was applied. A colour mask extracted the tracking points from the image. Canny edge detection extracted borders from the greyscale-masked image. Then the find contours algorithm extracts the borders and their central point.

IV. Experiment 1: Tissue Stiffness Sensing

A. Tissue Stiffness Sensing Experimental Method

This section's experiment aims to evaluate the sensor's stiffness sensing ability. To achieve this a set of phantoms of different stiffness were produced. These were then used to assess how the sensor output changes with pressure when in contact with samples of different stiffness. Finally, the sensor's ability to quickly sense stiffness using a neural network was investigated.

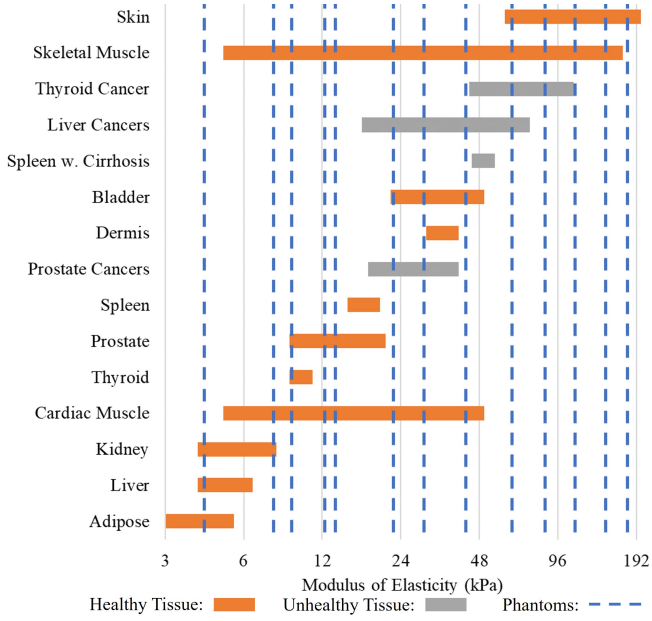

Fig. 2. The moduli of elasticity range of tissues and phantoms. The elasticity of a range of healthy (orange) and unhealthy (grey) tissues [10], [11], [35] are shown as horizontal bars, along with the moduli of elasticity of phantoms used in experiments, displayed as vertical dashed blue lines.

1) Soft Phantoms: To evaluate the sensor's ability to measure tissue stiffness, phantoms were produced in the stiffness range of human tissues. Many healthy human tissues, including the liver, prostate, and skin, have moduli of elasticity of between 3 kPa and 100 kPa [10]. Conditions such as liver fibrosis, papillary adenocarcinoma and prostate cancer have been shown to increase the stiffnesses of their respective healthy tissues by a factor of 1.9 to 9 [10], [35]. Therefore to demonstrate that our sensor could differentiate between different tissues and between healthy and unhealthy tissue, we created a range of phantoms with elasticities between 4 kPa and 180 kPa with an average step factor of 1.38. Fig. 2 illustrates phantom elasticity compared to a range of healthy and unhealthy tissues.

Phantoms of different stiffness were produced from Smooth-On platinum-cured silicone elastomers. Table II summarises the materials and ratios used to produce these phantoms, together with the modulus of elasticity obtained through compression testing. The silicone mixtures were degassed and cast into cylindrical phantoms of diameter 50 mm and height 30 mm identical to dimensions used in work by Omata et al. [15]. Compression testing was carried out on a Zwick/Roell Z1.0 with a 1 kN load cell. Phantoms were compressed 20% from a preload of 0.1 N. The modulus of elasticity was calculated over the first 10% compression. This was repeated 10 times per phantom, five times on each side. The first repetition on each side was removed giving a total of eight analysed repetitions per phantom. This produced 3976 lines of data per phantom which were used to calculate

TABLE II
SOFT PHANTOM MATERIALS AND ELASTICITIES

Ratio of Components	Elasticity	Ratio of Components	Elasticity
4 Ecoflex 00-10 Part A: 4 Ecoflex 00-10 Part B: 8 Silicone Thinner	4.20 kPa	4 Ecoflex 00-10 Part A: 4 Ecoflex 00-10 Part B: 7 Silicone Thinner	7.83 kPa
4 Ecoflex 00-10 Part A: 4 Ecoflex 00-10 Part B: 6 Silicone Thinner	9.12 kPa	4 Ecoflex 00-10 Part A: 4 Ecoflex 00-10 Part B: 5 Silicone Thinner	12.32 kPa
4 Ecoflex 00-10 Part A: 4 Ecoflex 00-10 Part B: 4 Silicone Thinner	13.35 kPa	4 Ecoflex 00-10 Part A: 4 Ecoflex 00-10 Part B: 3 Silicone Thinner	22.36 kPa
4 Ecoflex 00-10 Part A: 4 Ecoflex 00-10 Part B: 2 Silicone Thinner	29.27 kPa	4 Ecoflex 00-10 Part A: 4 Ecoflex 00-10 Part B: 1 Silicone Thinner	42.12 kPa
4 Ecoflex 00-10 Part A: 4 Ecoflex 00-10 Part B	63.62 kPa	4 Ecoflex 00-20 Part A: 4 Ecoflex 00-20 Part B	85.08 kPa
4 Ecoflex 00-30 Part A: 4 Ecoflex 00-30 Part B	111.41 kPa	4 Ecoflex 00-35 Part A: 4 Ecoflex 00-35 Part B	145.72 kPa
4 Ecoflex 00-50 Part A: 4 Ecoflex 00-50 Part B	177.62 kPa		

Phantoms shaded in grey are used in measuring displacement with internal pressure (section IV-A2) and for training, validation and testing in section IV-A3. Unshaded phantoms are used as untrained phantoms for testing in section IV-A3

the modulus of elasticity with a mean standard deviation of 0.431%.

2) Measuring Displacement with Internal Pressure: To understand how the displacement-internal pressure relationship varied with phantom elasticity, an experiment was set up to slowly inflate the membrane whilst continually monitoring the tracking point displacements. The sensor, secured in the gripper of a Franka Emika Panda robot, was positioned parallel to and concentric with, the phantom. Whilst the membrane was more than 10 mm above the phantom, the positions of the tracking points were recorded for calibration. After lubricating the phantom and membrane with a thin layer of oil, the sensor was lowered into contact with the phantom (Fig. 3a).

Contact, determined by the average displacement of the eight tracking points in the circle, was checked to be within a range of 24 pixels to 29 pixels. This range was chosen as it could be met on all phantoms within 20 calibration attempts and was at the upper limit that could be achieved on the softest phantom. Every five tests, the movement of the robot was reprogrammed in guide mode until the average displacement was within the previously mentioned range, ensuring a repeatable contact force.

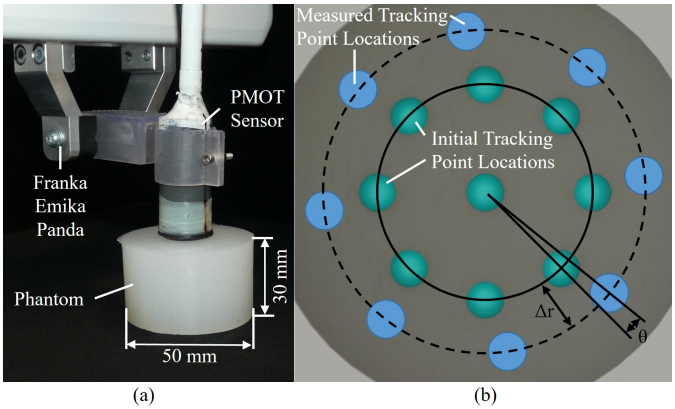

(a) (b)

Fig. 3. Tissue stiffness sensing experimental setup. (a) To sense stiffness, a robot lowered the PMOT sensor onto cylindrical elastomer phantoms and then the sensor was pressurised. (b) Tracking point locations are converted into polar coordinates to find the radial displacement (Δr) and angular displacement (θ) of each point.

Once in contact, the internal pressure was increased in steps of 0.061 kPa. After a 1 s pause at each step for membrane adjustment, tracking point locations were measured five times, with a 0.2 s gap between measurements, in line with our previous force-sensing procedure [27]. This was repeated up to a pressure of 9.77 kPa, then the experiment was reset. The experiment was repeated with every second phantom, shaded grey in Table II. Each phantom was tested five times, producing 805 lines of data per phantom.

Position data for each tracking point at each pressure was extracted and converted to polar coordinates around the central point measured as the radial displacement (Δr) in pixels (px) and angular displacement (θ) in degrees ($^\circ$). Δr measures the tracking point's change in distance from the centre point, whilst θ measures the change in angular displacement around a circumference with an origin at the central point (Fig. 3b). This allows tracking points' movements to be assessed whilst also allowing the effects of torsion on the membrane to be removed. The average radial displacement ($\overline{\Delta r}$) was obtained by averaging the Δr for all tracking points, except the centre point, at each measurement.

3) Stiffness Sensing Methodology: To reduce the time taken to measure tissue stiffness, sensing was carried out using four internal pressures of the sensor (0 kPa, 2 kPa, 4 kPa & 6 kPa). The experiment was set up in line with the procedure described in section IV-A2 and shown in Fig. 3. At each of the four pressures, the membrane was given 0.1 s to adjust; then, tracking point locations were measured four times with a 0.1 s gap between measurements. The adjustment time and measurement count were reduced from IV-A2 to decrease the sampling time to an average of 4.58 s. Data was extracted and converted to $\overline{\Delta r}$ using the method described in section IV-A2.

The experiment was repeated 24 times with every second phantom, shaded grey in Table II, to create training and validation datasets, 20 times for training and 4 times for validation. Giving a total of 140 lines of training data and 28 lines of validation data. The experiment was then repeated with every phantom 16 times to produce a testing dataset. Giving a total of 208 lines of testing data. Each experiment repetition produced a smaller amount of data and neural networks require a greater volume of data to train and test than other models. Therefore, more repetitions were used for this experiment than for the others.

4) Stiffness Sensing Neural Network Architecture and Training: A neural network (NN) was used to identify sample stiffness from sensor outputs. The architecture of the network is shown in Fig. 4. The average tracking point displacement at each pressure is input to the NN. The feed-forward fully connected regression NN has three hidden layers of five nodes each. Each node applies a linear activation function to its inputs based on weights established in training. The network was trained using the corresponding phantom elasticity, obtained from compression testing, as the ground

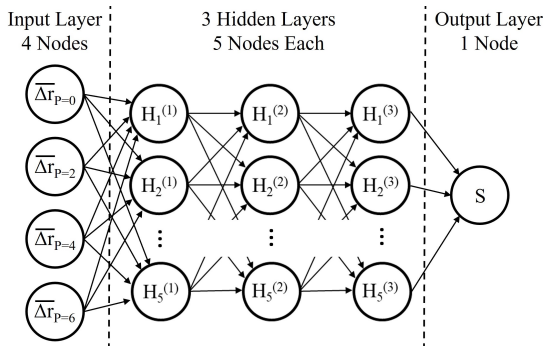

Fig. 4. Neural Network architecture showing inputs, nodes and outputs. Average radial displacements of tracking points ($\overline{\Delta r}$) at internal pressures of 0 kPa, 2 kPa, 4 kPa & 6 kPa were fed into 3 hidden layers of 5 fully connected nodes, from which the phantom stiffness was output.

truth output.

Before training, all data was standardised between -1 and 1. The network was built using the MATLAB fitrnet function. This function does not allow a batch size to be set, therefore all training data was used in each batch resulting in one iteration being the same as one epoch. The network was trained using a Limited-memory Broyden–Fletcher–Goldfarb–Shanno (L-BFGS) algorithm to carry out supervised learning with the results being compared to the validation data every five iterations. Training was repeated until the function loss was less than 1e-16. The trained NN produced an RMSE of 0.321 kPa on validation data. The neural network was tested using testing data, the results of which are reported in section IV-B2.

B. Tissue Stiffness Sensing Results

1) Measuring displacement, $\overline{\Delta r}$, with Internal Pressure: The $\overline{\Delta r}$ - internal pressure raw data is plotted for each of the phantoms in Fig. 5. The $\overline{\Delta r}$-pressure curve changes with the phantom stiffness. Table III shows the gradient of a linear fit of the points up to 1 kPa internal pressure for each of the phantoms. As the phantom stiffness increases, the gradient increases.

2) Stiffness Sensing: Testing data was input to the NN and the output was analysed to assess the stiffness sensing ability of the sensor. To quantify the accuracy of the sensor, the output was compared to the phantom stiffness to calculate the root-mean-square error (RMSE) and non-repeatability for each phantom and across ranges of phantoms. The average RMSE is 2.47 kPa, whilst the non-repeatability is 16.24% of the range. Table IV shows the RMSE at each phantom stiffness. The average RMSE for trained phantoms is 0.25 kPa and for untrained phantoms is 5.07 kPa (2.85% of range). For untrained data, a Pearson product-moment correlation coefficient showed that the accuracy of the sensor decreased as the phantom stiffness increased, $r(95) = 0.65, p < 0.001$. Additionally, we see an improvement in sensor performance if the range of the sensor is limited to 64 kPa, the average RMSE reduces to 0.98 kPa, whilst the non-repeatability becomes 4.68% of the range. To compensate for this non-linear behaviour, the RMSEs were also calculated as a % of the phantom stiffness of each reading, this is also shown in Table IV. The average % RMSE of all untrained phantoms was 7.72% of sample stiffness. To allow for comparison with papers that do not calculate the RMSE, the mean absolute errors (MAE) were calculated for all untrained phantoms. The MAE was 4.55 kPa, equivalent to 7.07% of sample stiffness or 2.56% of sensor range.

TABLE III
INITIAL PRESSURE-DISPLACEMENT GRADIENT (UP TO 1 KPA) VS PHANTOM STIFFNESS

	Phantom Stiffness (kPa)						
	4.20	9.12	13.35	29.27	63.62	111.41	177.62
Gradient (px/kPa)	-19.437	-13.934	-10.031	-3.650	0.486	1.709	2.0833

C. Tissue Stiffness Sensing Discussion

1) Measuring Displacement, $\overline{\Delta r}$, with Internal Pressure: Fig. 5 shows that the shape of the $\overline{\Delta r}$ - internal pressure curve changed with phantom stiffness. It can be seen that as the phantom stiffness increased, so did the initial gradient of the curve. This is further shown in Table III. Whilst the stiffness of the phantoms increases exponentially, the gradient does not, suggesting a non-linear relationship. These results suggest that the PMOT sensor will be able to sense phantom stiffness using

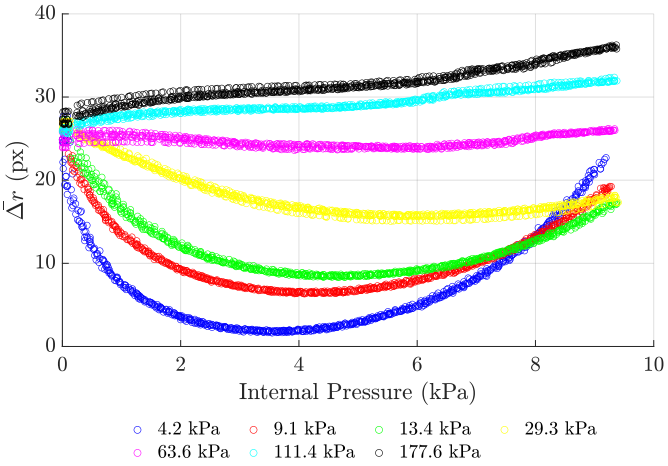

Fig. 5. Raw data for stiffness sensing using pressurisation when the sensor is in contact with the phantom. Tracking point displacement, $\overline{\Delta r}$, is graphed against the internal pressure of the sensor for different stiffness. Different stiffnesses of phantoms are represented by different coloured data points. The starting gradient of the line changes as the phantom stiffness increases.

TABLE IV
STIFFNESS SENSING ACCURACY

	Trained Phantom Stiffness (kPa)						
	4.20	9.12	13.35	29.27	63.62	111.41	177.62
RMSE (kPa)	0.205	0.059	0.224	0.218	0.778	0.224	0.031
RMSE (%)	4.883	0.651	1.682	0.746	1.224	0.201	0.018

	Untrained Phantoms Stiffness (kPa)					
	7.83	12.32	22.36	42.12	85.08	145.72
RMSE (kPa)	0.244	0.419	2.671	3.991	5.326	17.763
RMSE (%)	3.113	3.397	11.944	9.475	6.260	12.190

$\overline{\Delta r}$ at selected known pressures and that lower stiffnesses will be sensed more accurately than high stiffnesses.

2) Stiffness Sensing: The results in Table IV demonstrate that the PMOT sensor can measure phantom stiffness, especially at low stiffnesses allowing us to identify healthy and unhealthy soft tissues. The errors were higher for untrained phantoms than for trained phantoms. This shows that the model is biased towards data that is similar to its training set. This discrepancy could be reduced by introducing more intermediate training samples. As demonstrated by the Pearson product-moment correlation, increasing phantom stiffness increased errors. This is likely caused by the non-linear behaviour discussed in section IV-C1. The RMSE of each phantom is less than half of the interval to its neighbouring phantoms allowing the sensor to differentiate between all phantoms. The results were compared to other literature from section II. The RMSE for untrained phantoms was 2.85% of range. This is lower than the RMSE of 5.95% of range from [14]. The MAE was 7.07% of sample stiffness. This is comparable with mean errors between 3.5% and >10% of sample stiffness from other literature [2], [4], [13], [17]

V. Experiment 2: Dynamic Palpation on a Linear Rail

A. Linear Rail Palpation Method

The ability to detect margins, the edges of areas of different stiffnesses, is key to locating and measuring those areas. Experiments were carried out to evaluate the sensor's ability to sense margins during dynamic palpation on a linear rail. To do this stadium-shaped phantoms with a margin in the middle were produced. The sensor, mounted on a linear rail, was then moved across these phantoms, under different input parameters. Tracking point displacements converted to $\overline{\Delta r}$ were extracted throughout the movement.

1) Stadium-shaped Linear Rail Phantom Production: A range of stadium-shaped phantoms were produced from pairs of materials. Healthy and cancerous prostate tissues have average stiffnesses of 15.3 kPa and 28.8 kPa, respectively [35]. Therefore, elastomers of 13.4 kPa, 22.4 kPa and 29.3 kPa in stiffness, presented in Table II, were used to produce these phantoms. As shown in Fig. 6, each material filled half of the phantom. This was then covered in a layer of the softer material for a flat finish and variable embedded depth (D). The boundary where the materials meet mimics a surgical margin and will be referred to as such. Phantoms were created with different pairs of materials and embedded depths (D).

2) Linear Rail Palpation Methodology: The PMOT sensor was mounted on a linear rail above a phantom to control and acquire its position (see Fig. 6). The initial positions of the tracking points were measured. The phantom and membrane were lubricated with a thin layer of oil. Then, the sensor was pressurised, lowered to a preloaded force F_0, and moved over the phantom. The sensor was moved from 25 mm left to 25 mm right of the margin (Fig. 6 B to C) and back (moved from C to B) five times. At the end of each pass, the sensor was moved 5.9 mm away from the margin and back to reverse the direction of the shear (Fig. 6 SRM). The tracking

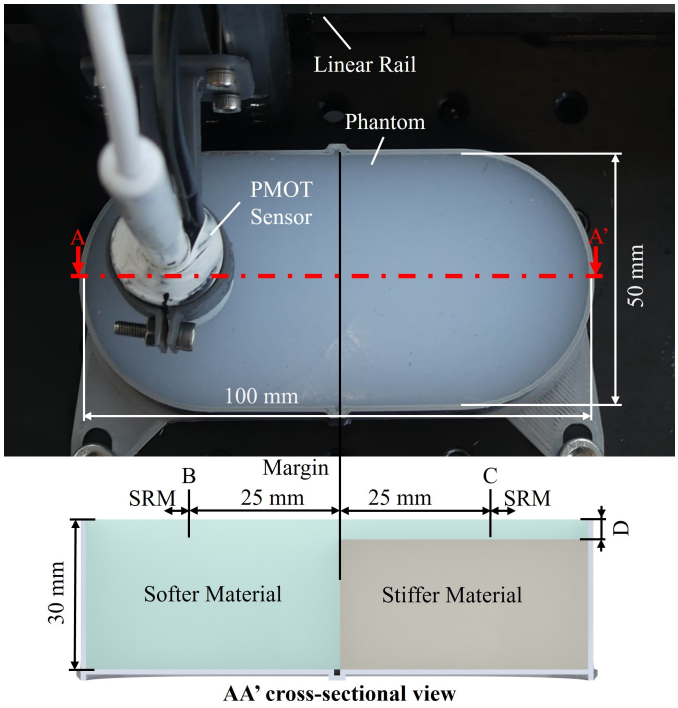

Fig. 6. Experimental setup for dynamic palpation on a linear rail. The PMOT sensor is moved over the phantom by a linear rail. B & C are the start and end points of each pass, whilst SRM represents the shear reversal movements. The phantom's dimensions and cross-section view are also illustrated. The embedded depth (D) is varied between trials.

point positions, linear rail position and internal pressure were sampled with a frequency of 5 Hz. Every five readings were averaged to mitigate outliers.

The experiment was repeated with different parameter combinations, denoted as configurations. The configurations and corresponding results are summarised in Table V. E_1 represents the stiffness of the softer material. E_2 indicates the stiffness of the stiffer embedded material. D stands for the depth that the stiff material is embedded below the soft material. P denotes the PMOT sensor's internal pressure. F_0 shows the force the sensor was preloaded to at the start of the experiment. Speed expresses the velocity of the linear rail. Sensor Orientation indicates if the sensor was mounted forward, with the top of the internal camera image towards the rail, or backwards, with the top of the camera image away from the rail. This is altered by rotating the PMOT sensor 180° inside its holder. Changing the sensor orientation swaps the leading and trailing edges of the sensor in each direction of movement.

Baseline parameters were determined through preliminary tests varying P (2 kPa to 5 kPa, steps of 0.5 kPa), F_0 (70 mN to 120 mN, steps of 0.25 mN), and speed (0.25 mm/s to 1 mm/s, steps of 0.25 mm/s). The parameters highlighted in grey in Table V were chosen as the baseline parameters due to having the highest signal-to-noise ratio (SNR) in preliminary testing.

For each configuration, the experiment was repeated 3 times, discarding the first pass in each direction, resulting in 12 passes per direction per configuration. This yielded an average of 3245 lines of data per configuration.

TABLE V
MARGIN SENSING TRIALS

	Input Parameters							Outputs					
Conf.	E_1	E_2	D	P	F_0	Speed	Sensor	Soft-Stiff			Stiff-Soft		
#	(kPa)	(kPa)	(mm)	(kPa)	(mN)	(mm/s)	Orientation	SNR, $\overline{\Delta r}$	SNR, F	Offset (mm)	SNR, $\overline{\Delta r}$	SNR, F	Offset (mm)
1	13.4	29.3	2	3.0	100	0.5	Forward	26.83:1	20.47:1	1.4663	38.85:1	40.04:1	2.9163
2	13.4	29.3	2	3.5	100	0.5	Forward	34.17:1	32.97:1	0.334	44.85:1	43.33:1	2.718
3	13.4	29.3	2	4.0	100	0.5	Forward	26.39:1	25.52:1	0.354	30.84:1	30.00:1	3.648
4	13.4	29.3	2	3.5	90	0.5	Forward	38.67:1	37.50:1	0.226	37.69:1	36.72:1	3.068
5	13.4	29.3	2	3.5	110	0.5	Forward	30.32:1	27.18:1	0.418	49.33:1	49.46:1	3.286
6	13.4	29.3	2	3.5	100	0.25	Forward	31.57:1	30.64:1	0.526	32.32:1	30.53:1	3.556
7	13.4	29.3	2	3.5	100	0.75	Forward	34.15:1	31.89:1	0.241	34.42:1	33.2:1	3.245
8	13.4	29.3	2	3.5	100	0.5	Backward	22.27:1	20.12:1	0.373	27.94:1	26.04:1	2.91
9	13.4	22.4	2	3.5	100	0.5	Forward	26.53:1	26.37:1	0.902	14.89:1	14.83:1	2.624
10	13.4	22.4	2	3.0	100	0.5	Forward	25.27:1	24.69:1	0.625	18.20:1	17.81:1	2.093
11	13.4	22.4	2	3.5	90	0.5	Forward	22.74:1	22.72:1	1.244	11.09:1	11.18:1	1.578
12	22.4	29.3	2	3.5	100	0.5	Forward	10.88:1	10.79:1	0.987	5.37:1	5.39:1	0.761
13	22.4	29.3	2	4.0	100	0.5	Forward	8.55:1	8.41:1	1.019	4.27:1	4.33:1	1.448
14	22.4	29.3	2	3.5	110	0.5	Forward	12.14:1	12.11:1	0.697	6.13:1	6.13:1	0.837
15	13.4	29.3	4	3.5	100	0.5	Forward	42.39:1	41.04:1	0.195	18.69:1	18.05:1	1.763
16	13.4	29.3	6	3.5	100	0.5	Forward	30.86:1	30.59:1	1.171	13.11:1	13.07:1	1.344

1. Configuration 2, highlighted in grey, contains the baseline parameters.
2. The parameter being varied in each test is highlighted in orange.
3. E_1 and E_2 are the moduli of elasticity of the softer and stiffer material, respectively.
4. Soft-Stiff results are obtained by passing the sensor from the softer to the stiffer material (Fig. 6 0 to 1).
5. Stiff-Soft results are obtained by passing the sensor from the stiffer to the softer material (Fig. 6 1 to 0).
6. Offset is the distance between the margin and the middle of the signal.

3) Linear Rail Palpation Data Processing: The position of the sensor and internal pressure were extracted for each reading. Tracking point locations were extracted and converted into $\overline{\Delta r}$ in line with section IV-A2. Due to the large shear forces exerted on the membrane during the experiment, $\overline{\Delta r}$ was adjusted for stability. This was done by adjusting the tracking points positions relative to the central point and applying a linear adjustment to $\overline{\Delta r}$ based on the central tracking point's displacement. The force on the sensor in Newtons was calculated from $\overline{\Delta r}$ using a 4th-order polynomial relationship obtained through the method described in our previous work [27].

B. Linear Rail Palpation Results

The signal-noise ratio (SNR) was obtained for each pass of the sensor over the margin, the position of which is known, in line with the work by McKinley et al. [19]. The signal segment comprised points within a 20 mm range centred on the margin. The points on either side of this section were extracted as the upper and lower noise segments. Fig. 7a displays these segments on a force graph for a sensor pass over the margin from the softer material to the stiffer material. The SNR was determined by dividing the amplitude of the signal segment by the root-mean-square deviation (RMSD) of the noise segments. The offset between the centre of the sensor passing over the margin, and the middle of the signal was calculated. A linear fit was applied to 16 points centred on half the signal amplitude. The fit was then used to find the position where the line intercepted half the signal amplitude. The difference in mm between this position and the margin location was defined as the offset. The offset is shown in Fig. 7b on a force graph for a sensor pass over the margin from the stiffer material to the softer material.

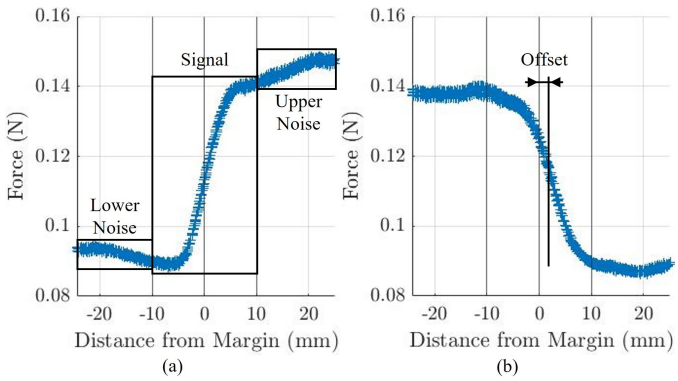

Fig. 7. As the sensor is moved over the margin by the linear rail, the force measured by the sensor changes. (a) The amplitude of the signal and RMSD of the noise were extracted to find the SNR. (b) The distance from the margin where the measured force changed by half the signal amplitude was interpreted as the offset.

The SNR for raw $\overline{\Delta r}$ data and calculated force, as well as the offset, were averaged for each sample, in each direction. These results are shown alongside experimental parameters in Table V, where soft-stiff denotes a pass from the softer material to the stiffer material and stiff-soft denotes a pass from the stiffer material to the softer material. The baseline configuration chosen from preliminary tests is shown in grey (config. 2).

C. Linear Rail Palpation Discussion

Adjusting the internal pressure (config. 1 & 3) or speed (config. 6 & 7) decreases the average SNR (both $\overline{\Delta r}$ and force). This shows that the baseline conditions are close to a local optimum for this phantom and that adjusting these parameters affects the sensor's ability to locate the margin. Averaging between directions of passes in these conditions gives an SNR from $\overline{\Delta r}$ of 39.51:1 and an offset of 1.526 mm.

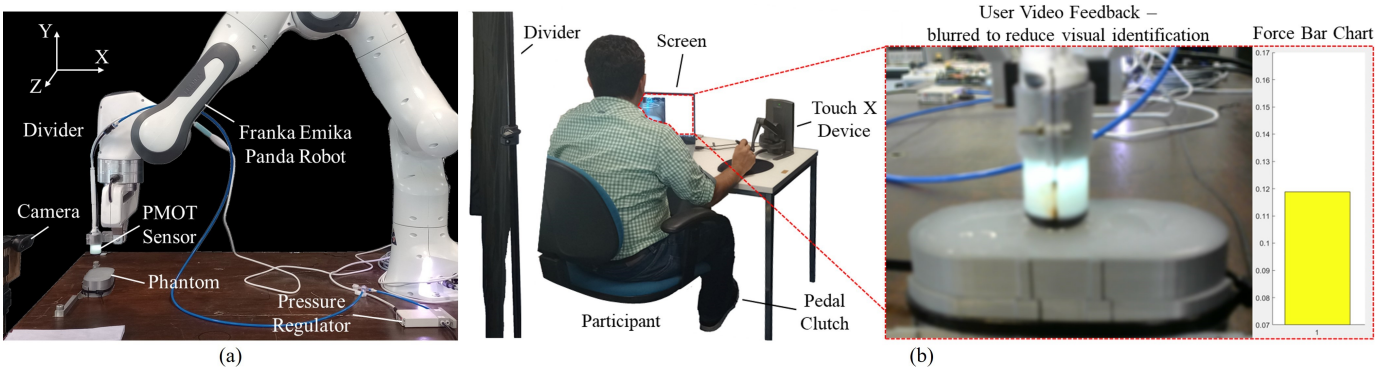

Fig. 8. Experimental setup for teleoperated dynamic palpation. Participants control the palpation of the sensor using a teleoperation system. The properties of the margin were identified using a force bar chart from the PMOT sensor. (a) The responder side of the experiment is where the sensor and phantom are located. (b) The controller side of the experiment is where the participant is positioned.

Reducing the preload force (config. 4) decreases average SNR. However, when the preload force is increased (config. 5), the average SNR from $\overline{\Delta r}$ increases by 0.786%. Additionally, the difference between the SNR with direction is exacerbated and the average offset becomes 21.4% larger. This shows that when adjusting the preload there is a trade-off between increasing in average SNR and increasing the offset and directional sensitivity. Additionally, the increased offset with a larger force suggests that the larger force intensifies the friction and shear forces on the membrane.

Orientating the sensor backwards (config. 8) deteriorates all results. The stiff-soft SNR to soft-stiff SNR ratio is similar to the baseline. This suggests the sensor orientation has little effect on the change in SNR with direction of travel. The signal amplitude and offset are similar between configurations 8 and the baseline. The reduced SNRs are due to an increase in the noise, especially at the stiff end of the phantom. When the sensor orientation was rotated, it changed the forces acting on the pneumatic piping. This may have caused forces to be transferred from the pipe to the sensor, especially at the far end of the movement, moving the sensor and increasing the noise. This could be reduced by increasing the security of the hold on the sensor and the pipes. Softer pipes may reduce transmitted forces but increase the chances of pipes being pinched.

Decreasing the difference in elasticity between the softer and stiffer materials decreased the SNR. This was done by decreasing the stiffness of the stiffer material and increasing the stiffness of the softer material (config. 9 & 12). In both scenarios, the soft-stiff offset increased and the stiff-soft offset decreased; this demonstrates that in the soft-stiff offset the margin counteracts the effect of the shear whilst for the stiff-soft offset the margin exacerbates the effect of the shear.

When the stiffness of the stiffer material is decreased, decreasing the pressure of the sensor (config. 10) increases the average SNR whilst decreasing the force (config. 11) decreases it. Conversely, when the stiffness of the softer material is increased, increasing the pressure of the sensor (config. 13) increases the average SNR whilst decreasing the force (config. 14) increases it. This shows that whilst the internal pressure and initial force can be adjusted to optimise performances on different tissues, the relationship is complex and requires detailed study. The average SNR decreases as the embedding depth of the stiff material increases (config. 15 & 16).

The effects of the direction of the pass on the SNR were analysed. For configurations 1-3 and 5-8 the SNR was higher for the stiff-soft pass than the soft-stiff pass. In these configurations, during the soft-stiff pass, the noise increases from the soft side to the stiff side. The noise then decreases after the shear reversal movement on the stiff side in the stiff-soft pass. The noise decreases again when on the soft side to below that observed in the soft-stiff movement. This results in the soft-stiff noise being higher than the stiff-soft noise. The signal is slightly lower in the stiff-soft pass than the soft-stiff pass, but this is offset by the much larger change in noise.

The SNR was higher for the soft-stiff pass than the stiff-soft pass in configurations 4 and 9-16. In these configurations, the soft-stiff noise on the stiff side decreased whilst the stiff-soft noise on the stiff side increased compared to configurations 1-3 and 5-8. The force between the sensor and the stiff side of the sample was lower than in configurations 4 and 9-16 than in configurations 1-3 and 5-8. No clear correlations were found between noise and force, central tracking point displacement, or the change in central tracking point displacement.

VI. Experiment 3: Dynamic Palpation Using Teleoperation

A. Teleoperated Palpation Method

This experiment aims to determine if participants could use the sensor to locate margins in a teleoperation environment. To do this stadium-shaped phantoms with offset margins were created (similar to Fig. 6). A teleoperation setup was also produced by connecting a haptic device to a robot and relaying the force from the sensor to a graphical display (Fig. 8a & b). Participants then used the sensor in the teleoperated setup to determine the location of the margin and stiffer material within the phantom. This experiment was carried out under UCL Ethics ID 23899/001.

1) Phantoms Fabrication for Teleoperated Palpation: Stadium-shaped phantoms with the same dimensions as those described in section V-A1 were produced from 13.4 kPa and 29.3 kPa elastomers. Margins in these phantoms were

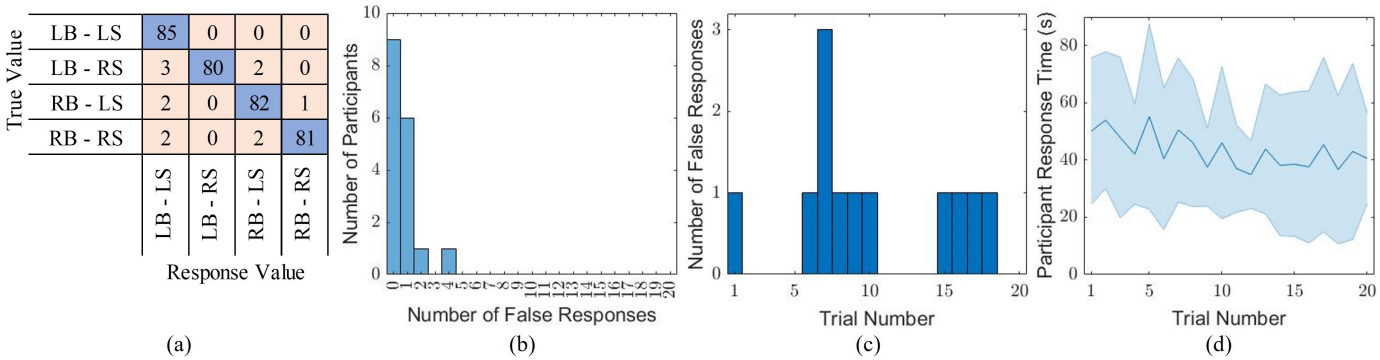

Fig. 9. Results from dynamic palpation using teleoperation. (a) Confusion matrix of true values vs those predicted by participants in teleoperated palpation experiment. LM and RM signify the margin being on the left or right of the phantom, respectively, while LS and RS signify the stiffer material is on the left or right of the phantom, respectively. (b) The distribution of false responses across participants. (c) The number of false responses across the 20 trials. (d) Average (μ) and standard deviation (σ) of the participant's response time across the 20 trials.

positioned 10 mm to one side of the centre to produce four different combinations of properties: margin left or right of the centre, and stiffer material left or right of the margin. The stiffer material was embedded 2 mm below the softer material.

2) Teleoperation Setup: The teleoperation setup consisted of a Franka Emika Panda seven-degree-of-freedom articulated arm robot on the responder side (Fig. 8a) and a 3D Systems Geomagic Touch X haptic device on the controller side (Fig. 8b). Robot Operating System (ROS) integrated the haptic device, the robot, and a pedal clutch. When the clutch was pressed, Cartesian space mapping translated haptic device pen movements to the robot, which was moved with a torque impedance controller.

The PMOT sensor was mounted in the gripper of the Panda robot. Data from the sensor was converted into force data using the method described in section V-A3. Forces were displayed to the participant in a colour-changing bar chart going from 0.07 N to 0.17 N, in line with the range observed in Experiment 2. The red, green and blue (RGB) colour values of the graph [0 1 0.1], [1 1 0.1] and [1 0 0.1] were fitted linearly to the force values 0.07 N, 0.12 N, and 0.17 N, respectively. This colour change was applied to make the graph more intuitive to read.

A phantom was secured on the table below the sensor (see Fig. 8). A camera was positioned to feed a video of the sensor and the phantom to the participant during palpation. Using OpenCV, a 10 px by 10 px blur was applied to the camera video to reduce visual phantom identification. The operator workstation on the controller side contained a seat for the participant, the pedal clutch, the Touch X device and a monitor showing the blurred video and force bar chart. A black fabric screen divider was placed between the participant and the responder side of the experiment to prevent extra visual cues. Before the experiment, a thin layer of oil was applied to the sensor and the phantoms for lubrication.

3) Dynamic Palpation Using Teleoperation Methodology: The experiment was conducted with 17 participants, 8 male and 9 female, ranging from 19 to 40 years in age, with a mean age of 29 years. Participants had no sensory or motor impairments. The setup and aim of the experiment were explained to the participants before they were seated at the operator workstation. The phantom was secured on the table, and the PMOT sensor was positioned over its centre. Participants palpated the phantom, moving the PMOT sensor vertically and horizontally parallel to the camera (Y and Z axes in Fig. 8a). Participants were asked to identify the location and stiffer side of the margin by palpating the phantom and observing the corresponding forces. Participants could practice with two phantoms of known properties to familiarise themselves with the teleoperation system and using the sensor for palpation. After this, participants were presented with phantoms in 20 randomised trials. MATLAB code using the randi function ensured each of the four phantoms was used five times. For each phantom, the participant's response was recorded, as well as the time. Participants were given a 2 minute limit to palpate each phantom, at which point the teleoperation system would stop and a response would be requested. This method was designed to produce the maximum amount of data whilst ensuring the experiment would not use over one hour of the participant's time.

B. Teleoperated Palpation Results

Participant responses during palpation were compared to true values in a confusion matrix, Fig. 9a. Where the location of the margin on the left or right of the phantom is signified by LM and RM, respectively. The location of the stiffer material, left or right of the margin, is signified by LS and RS, respectively. The sensor's accuracy was 96.5%, whilst the average response time was 42.9 s. Average response time for each combination, LM-LS, LM-RS, RM-LS, & RM-RS were 36.2 s, 48.5 s, 43.9 s, & 44.6 s respectively.

To analyse how false responses varied with each participant, Fig. 9b graphs the number of false responses against the number of corresponding participants. To understand how participants' performance changed throughout the experiment, the number of false responses and average time to give a response were graphed against the trial number in Fig. 9c & d, respectively. A Pearson product-moment correlation coefficient showed that as participants conducted more trials, response times decreased, $r(340) = -0.147, p = 0.007$.

C. Teleoperated Palpation Discussion

Fig. 9a highlights the sensor's capability of identifying margins during teleoperated palpation. False responses were spread between all values apart from LM-LS, aligning with the average response time of LM-LS being shorter. The higher false response rate for phantoms with larger stiff sections, LM-RS & RM-LS, indicates that starting palpation on stiffer material or having larger stiffer areas may decrease margin detection accuracy. Fig. 9b demonstrated that all users understood the sensor output with nine of the 17 participants made no false responses and only two making more than one false response. This underscored that all users could understand the sensor output.

Fig. 9c indicates a lack of reduction in false responses over trials, possibly due to the absence of feedback hindering accuracy improvement. Nevertheless, with increased trials, participants got used to the teleoperation system and sensor, decreasing response times. This is shown in Fig. 9d and through the Pearson product-moment correlation.

VII. Conclusion and Future Work

This paper presented a soft-tipped sensor for quantifying phantom elasticity and locating changes in stiffness during dynamic palpation. Results demonstrate that the PMOT sensor can measure the tissue stiffness of samples between 4.20 kPa and 177.62 kPa using a novel method of pneumatically adjusting its compliance and measuring the corresponding deformation. On untrained phantoms the sensor achieves an average RMSE of 7.72% of sample stiffness, demonstrating that the sensor can differentiate between the silicone elastomer phantoms, representing healthy and unhealthy tissues with an average step factor of 1.38.

The PMOT sensor, functioning as a force sensor, could also detect margins between 13.4 kPa elastomer and 29.3 kPa embedded elastomer during dynamic palpation. On a linear rail, the sensor achieved an average SNR of 39.5:1 and an average offset of 1.53 mm under conditions close to a local optimum. When carrying out palpation using the sensor mounted on a teleoperated robot, participants could detect the margin and stiffer elastomer locations with an accuracy of 96.5%.

In future work, the sensor will be miniaturised. This will reduce the offset in margin detection caused by shear on the membrane and allow the sensor to be used in minimally invasive surgery applications. Alternative machine learning and mathematical models should be explored to enhance stiffness sensing. This should be coupled with an analysis of how the quantity and distribution of training samples impact the performance of the sensor in stiffness sensing. The palpation capabilities of the sensor will be investigated further by altering variables such as the margin shape, the margin angle, elastomers' stiffness and phantom shape. This should be coupled with further studies to create a more detailed image of the sensor's palpation performance. Analysing using different samples and increasing the range of internal pressures and preload forces used. Usage duration should also be investigated to determine the effect of drift on the sensor's performance. Finally, the sensor should be integrated into a teleoperated haptic feedback system and user's palpation accuracy should be assessed.

References

[1] A. M. Handorf, Y. Zhou, M. A. Halanski, and W. J. Li, "Tissue stiffness dictates development, homeostasis, and disease progression," *Organogenesis*, vol. 11, no. 1, pp. 1–15, 2015.

[2] A. Faragasso, A. Stilli, J. Bimbo, Y. Noh, H. Liu, T. Nanayakkara, P. Dasgupta, H. A. Wurdemann, and K. Althoefer, "Endoscopic add-on stiffness probe for real-time soft surface characterisation in mis," *2014 Annu. Int. Conf. IEEE Eng. Med. Biol. Soc.*, pp. 6517–20, 2014.

[3] G. P. Jenkinson, A. T. Conn, and A. Tzemanaki, "Espress.0: Eustachian tube-inspired tactile sensor exploiting pneumatics for range extension and sensitivity tuning," *Sensors*, vol. 23, no. 2, 2023.

[4] A. Faragasso, J. Bimbo, A. Stilli, H. A. Wurdemann, K. Althoefer, and H. Asama, "Real-time vision-based stiffness mapping," *Sensors*, vol. 18, no. 5, 2018.

[5] M. Li, T. Ranzani, S. Sareh, L. D. Seneviratne, P. Dasgupta, H. Wurdemann, and K. Althoefer, "Multi-fingered haptic palpation utilizing granular jamming stiffness feedback actuators," *Smart Materials and Structures*, vol. 23, no. 9, p. 095007, jul 2014.

[6] A. Hassanbeiglou, M. Kalantari, E. Mozaffari, J. Dargahi, and J. Kövecses, "A new tactile array sensor for viscoelastic tissues with time-dependent behavior," *Sens. Rev.*, vol. 35, no. 4, pp. 374–381, 2015.

[7] M. Hollenstein, G. Bugnard, R. Joos, S. Kropf, P. Villiger, and E. Mazza, "Towards laparoscopic tissue aspiration," *Med. Image Anal.*, vol. 17, no. 8, pp. 1037–45, 2013.

[8] Y. Zhang, F. Ju, X. Wei, D. Wang, and Y. Wang, "A piezoelectric tactile sensor for tissue stiffness detection with arbitrary contact angle," *Sensors*, vol. 20, no. 22, 2020.

[9] T.-V. Nguyen, R. Tanii, T. Takahata, and I. Shimoyama, "Development of a single-chip elasticity sensor using mems-based piezoresistive cantilevers with different tactile properties," *Sens. Actuators A: Phys.*, vol. 285, pp. 362–368, 2019.

[10] C. F. Guimarães, L. Gasperini, A. P. Marques, and R. L. Reis, "The stiffness of living tissues and its implications for tissue engineering," *Nat. Rev. Mater.*, vol. 5, no. 5, pp. 351–370, 2020.

[11] R. Masuzaki *et al.*, "Assessing liver tumor stiffness by transient elastography," *Hepatol. Int.*, vol. 1, no. 3, pp. 394–7, 2007.

[12] E. Afshari, H. Sarkhosh, and S. Najarian, "A novel tactile probe with medical and surgical applications," *Sens. Rev.*, vol. 37, no. 4, pp. 404–409, 2017.

[13] M. M. Gubenko *et al.*, "Video-tactile pneumatic sensor for soft tissue elastic modulus estimation," *Biomed. Eng. Online*, vol. 16, no. 1, p. 94, 2017.

[14] W. Yuan, C. Zhu, A. Owens, M. A. Srinivasan, and E. H. Adelson, "Shape-independent hardness estimation using deep learning and a gelsight tactile sensor," *IEEE Int. Conf. Robot. and Autom.*, pp. 951–958, 2017.

[15] S. Omata, Y. Murayama, and C. E. Constantinou, "Real time robotic tactile sensor system for the determination of the physical properties of biomaterials," *Sens. Actuators A: Phys.*, vol. 112, no. 2-3, pp. 278–285, 2004.

[16] T. Nagatom and N. Miki, "A flexible tactile sensor to detect stiffness distribution without measuring displacement," *20th Int. Conf. Solid-State Sens. Actuators Microsyst. Eurosensors*, pp. 551–555, 2019.

[17] A. Faragasso, J. Bimbo, A. Yamashita, and H. Asama, "Disposable stiffness sensor for endoscopic examination," *2018 Annu. Int. Conf. IEEE Eng. Med. Biol. Soc.*, pp. 4309–4312, 2018.

[18] P. Puangmali, H. Liu, K. Althoefer, and L. D. Seneviratne, "Optical fiber sensor for soft tissue investigation during minimally invasive surgery," *IEEE Int. Conf. Robot. Autom.*, 2008.

[19] S. McKinley *et al.*, "A single-use haptic palpation probe for locating subcutaneous blood vessels in robot-assisted minimally invasive surgery," *IEEE Int. Conf. on Autom. Sci. Eng.*, 2015.

[20] J. Konstantinova, G. Cotugno, P. Dasgupta, K. Althoefer, and T. Nanayakkara, "Palpation force modulation strategies to identify hard regions in soft tissue organs," *PLoS One*, vol. 12, no. 2, p. e0171706, 2017.

[21] N. Herzig, P. Maiolino, F. Iida, and T. Nanayakkara, "A variable stiffness robotic probe for soft tissue palpation," *IEEE Robot. Autom. Lett.*, vol. 3, no. 2, pp. 1168–1175, 2018.

[22] U. Kim, Y. B. Kim, D.-Y. Seok, J. So, and H. R. Choi, "A surgical palpation probe with 6-axis force/torque sensing capability for minimally invasive surgery," *IEEE Trans. Ind. Electron.*, vol. 65, no. 3, pp. 2755–2765, 2018.
[23] M. Li, H. Liu, A. Jiang, L. D. Seneviratne, P. Dasgupta, K. Althoefer, and H. Wurdemann, "Intra-operative tumour localisation in robot-assisted minimally invasive surgery: A review," *Proc. Inst. Mech. Eng. H: J. Eng. Med.*, vol. 228, no. 5, pp. 509–522, 2014.
[24] A. Faragasso, A. Stilli, J. Bimbo, H. Wurdemann, and K. Althoefer, "Multi-axis stiffness sensing device for medical palpation," *2015 IEEE/RSJ Int. Conf. Intell. Robots Syst.*, pp. 2711–2716, 2015.
[25] S.-A. Abad, S. Homer-Vanniasinkam, and H. A. Wurdemann, "Chapter 4 - soft robotic systems for endoscopic interventions," in *Endorobotics*, L. Manfredi, Ed. Academic Press, 2022, pp. 61–93.
[26] K.-W. Kwok, H. Wurdemann, A. Arezzo, A. Menciassi, and K. Althoefer, "Soft robot-assisted minimally invasive surgery and interventions: Advances and outlook," *Proceedings of the IEEE*, vol. 110, no. 7, pp. 871–892, 2022.
[27] D. G. Raitt, S.-A. Abad, S. Homer-Vanniasinkam, and H. A. Wurdemann, "Soft, stiffness-controllable sensing tip for on-demand force range adjustment with angled force direction identification," *IEEE Sens. J.*, vol. 22, no. 9, pp. 8418–8427, 2022.
[28] O. Belyaev, H. Herden, J. J. Meier, C. A. Muller, M. H. Seelig, T. Herzog, A. Tannapfel, W. E. Schmidt, and W. Uhl, "Assessment of pancreatic hardness-surgeon versus durometer," *J Surg Res*, vol. 158, no. 1, pp. 53–60, 2010.
[29] J. D. Pampush, D. J. Daegling, A. E. Vick, W. S. McGraw, R. M. Covey, and A. J. Rapoff, "Technical note: Converting durometer data into elastic modulus in biological materials," *Am. J. Phys. Anthropol.*, vol. 146, no. 4, pp. 650–653, 2011.
[30] W. Yuan, S. Dong, and E. H. Adelson, "Gelsight: High-resolution robot tactile sensors for estimating geometry and force," *Sensors*, vol. 17, no. 12, 2017.
[31] X. Jia, R. Li, M. A. Srinivasan, and E. H. Adelson, "Lump detection with a gelsight sensor," *World Haptics Conf.*, pp. 175–179, 2013.
[32] A. Faragasso, J. Bimbo, Y. Noh, A. Jiang, S. Sareh, H. Liu, T. Nanayakkara, H. A. Wurdemann, and K. Althoefer, "Novel uniaxial force sensor based on visual information for minimally invasive surgery," *2014 IEEE Int. Conf. Robot. Autom*, pp. 1405–1410, 2014.
[33] A. Ali, K. Althoefer, and J. Konstantinova, "Dynamic response characteristics in variable stiffness soft inflatable links," *Towards Auton. Robot. Syst.*, pp. 160–170, 2019.
[34] J. Shi, A. Shariati, S.-A. Abad, Y. Liu, J. S. Dai, and H. A. Wurdemann, "Stiffness modelling and analysis of soft fluidic-driven robots using lie theory," *Int J Rob Res*, 2023.
[35] B. Ahn, E. I. Lorenzo, K. H. Rha, H. J. Kim, and J. Kim, "Robotic palpation-based mechanical property mapping for diagnosis of prostate cancer," *J Endourol*, vol. 25, no. 5, pp. 851–7, 2011.

VIII. Biography Section

Duncan G. Raitt received an MEng degree in Mechanical Engineering with international study from the University of Strathclyde, Scotland in 2019. He is currently pursuing a PhD degree in robotic sensing from University College London, UK. His main research interests include haptics and soft robotics.

Mahmud Huseynov received a BEng degree in Mechanical Engineering from University of Nottingham, UK. He later continued his education with an MSc in Robotics and Computation at University College London, UK. His main research interests include industrial and manufacturing robots.

Shervanthi Homer-Vanniasinkam is a Consultant Vascular Surgeon at Leeds Teaching Hospitals NHS Trust, the Founding Professor of Surgery at the University of Warwick Medical School & University Hospitals Coventry and Warwickshire, and Professor of Engineering & Surgery at University College London. She has published over 150 papers and book chapters, delivered over 300 presentations and has a significant research grant portfolio with an outstanding track record of national and international collaborative research. She is a Visiting Scholar at Harvard University, the Yeoh Ghim Seng Visiting Professor of Surgery at the National University of Singapore and the Brahm Prakash Visiting Professor at the Indian Institute of Science.

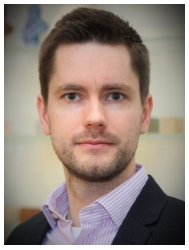

Helge A Wurdemann is Professor of Robotics at University College London leading the Soft Haptics and Robotics lab. Prior, he received a degree (Dipl.-Ing.) in electrical engineering with a focus on mechatronics and robotics in the medical field from the Leibniz University of Hanover, and a PhD in Robotics from King's College London in 2012. Helge has authored over 100 articles, published in high-impact journals, peer-reviewed full-length conference papers, and presented at leading robotics conferences.

Sara-Adela Abad is a Lecturer in Robotics at University College London, UK. In 2019, she received her PhD in Design Engineering and Robotics from Imperial College London, UK. She obtained her MSc in AI from the University of Southampton, UK and a BEng degree in Electronic and Control Engineering from the National Polytechnic School, Ecuador. Her research interests include bioinspired robotics, soft robotics, and robots' adaptability to uncertain conditions.